Disclaimer

This document was prepared as an account of work sponsored by an agency of the United States government. Neither the United States government nor Lawrence Livermore National Security, LLC, nor any of their employees makes any warranty, expressed or implied, or assumes any legal liability or responsibility for the accuracy, completeness, or usefulness of any information, apparatus, product, or process disclosed, or represents that its use would not infringe privately owned rights. Reference herein to any specific commercial product, process, or service by trade name, trademark, manufacturer, or otherwise does not necessarily constitute or imply its endorsement, recommendation, or favoring by the United States government or Lawrence Livermore National Security, LLC. The views and opinions of authors expressed herein do not necessarily state or reflect those of the United States government or Lawrence Livermore National Security, LLC, and shall not be used for advertising or product endorsement purposes.

Effect of Void Positioning on the Detonation Sensitivity of a Heterogeneous Energetic Material

Christopher Coffelt[a], Daniel Olsen[a], Christopher Miller[b], and Min Zhou[a]*

a) *The George W. Woodruff School of Mechanical Engineering and The School of Materials Science and Engineering, Georgia Institute of Technology, Atlanta, Georgia 30332-0405, USA*
b) *Lawrence Livermore National Laboratory, 7000 East Avenue, Livermore, CA. 94550 USA*

Abstract: Although it is well-established that voids profoundly influence the initiation and reaction behaviors of heterogeneous energetic materials such as polymer-bonded explosives (PBX) and propellants, there has been little study of how void location in different constituents in the microstructures of such materials affect the macroscale behavior. Here, we use three-dimensional (3D) mesoscale simulations to study how void placement within the reactive grains versus the polymer binder influences the shock-to-detonation transition (SDT) in a polymer-bonded explosive. The material studied here has a microstructure comprised of 75% PETN (pentaerythritol tetranitrate) grains and 25% HTPB (hydroxyl-terminated polybutadiene) polymer binder by volume. Porosities up to 10% in the form of spherical voids distributed in both the grains and polymer are considered. An Arrhenius reactive burn relation is used to model the chemical kinetics of the PETN grains under shock loading, thereby resolving the heterogeneous detonation behavior of the PBX. The influence of void location on the shock initiation sensitivity of the material is quantitatively ranked by comparing the predicted run distance to detonation (RDD) for each sample. The analysis includes inherent quantification of uncertainties arising from the stochastic variations in the microstructure morphologies and void distributions by using statistically equivalent microstructure sample sets (SEMSS), leading to probabilistic formulations for the RDD as a function of shock pressure. The calculations reveal that the location of voids in the composite microstructure significantly affects the RDD. Specifically, voids exclusively within the grains cause the PBX to be more sensitive (having shorter RDD) than voids in the polymer binder. Unique probabilistic relationships are derived to map the probability of observing RDD for each void location material case, allowing for prediction of initiation behavior anywhere in the shock pressure – RDD space. These findings agree with trends reported in the literature.

Introduction

The influence of microstructure heterogeneity on the shock-to-detonation transition (SDT) in high explosives (HEs) is of particular interest to the energetics community. 'Hot spots', or regions of localized temperature spikes, are often generated at defect locations in HEs subjected to shock loading and are widely understood to be a fundamental driving force in the detonation process [1, 2]. Micro and nanoscale defects, including voids and cracks, are present in all real samples, and are the most probable sites for hot spots to form [3-9]. As such, they profoundly affect the shock initiation behavior of the materials. The location of voids relative to the HE grains and polymer binder are important, as are the concentration and size of the void distribution. Although the shock initiation of HEs and the effects of voids in general have been extensively studied both in simulation [10-14] and experiments [2, 15-17], there has been no study on how the void location, whether in grains, binder, or some combination thereof, influences the detonation behavior on millimeter scale sample sizes. Understanding these influences on the sensitivity of the energetic materials is highly desirable to the larger HE community.

Characterizing voids in experimental samples is a challenging endeavor. Many experiments have been conducted to study the macroscale effects of voids via low density single or multi-crystal SDT [18-20], but without specific knowledge of individual voids within the material, it is impossible to correlate their effects with the observed behavior.

* Corresponding author, *e-mail address*: min.zhou@gatech.edu (M. Zhou).

The most common method for measuring pore distribution within a sample uses ultra-small angle X-ray scattering (USAXS) to measure void size, shape, volume and surface area. Unlike some more traditional scanning electron microscope (SEM) imaging techniques [21], USAXS is non-destructive and can provide a statistical representation of the current void density within a sample [22-24]. Willey et al. used USAXS data to measure how the void distribution evolved in several HMX-based formulations as they were heated [25] and TATB-based formulations as they were thermally cycled [26]. Mang and Hjelm [27] recently used USAXS to identify preferred void orientations in uniaxially pressed PBX 9502. While characterization of voids in samples has improved in recent years, the main method for understanding their impact on SDT largely remains a computational modeling effort.

Many simulations have focused on modeling the effects of the collapse of a single pore or smaller cluster of voids in a homogeneous energetic matrix. Li et al. [28] recently investigated the effect of geometry of single pores on the local temperature fields in HMX after shock induced collapse. Austin et al. [29] modeled a single pore collapse accounting for the crystal anisotropy of HMX and studied the resulting shear banding. Springer et al. [30] used the Lawrence Livermore National Laboratory (LLNL) hydrocode ALE3D to model the collapse of several pores in an HMX grain and demonstrated a shielding effect on downstream pores from upstream pores. This work additionally examined the hot spot evolution of individual voids both near and far from the grain border. Udaykumar et al. [31-34] studied the collapse of a single void, clusters of voids, and the reaction initiation behavior of porous granular HMX prepared by Molek et al. [35-37] While these studies have provided important insight into pore collapse and interactions among clusters of voids, few large-scale simulations have been attempted to model the entire impact, shock propagation, reaction initiation, and transition-to-detonation process using large-scale three-dimensional microstructures with explicit account of voids and microstructure so that the full mm size scale of the events can be captured. Miller et al. [38] initiated such an effort to model pressed granular HMX microstructures at the overall millimeter size scale. Although randomly distributed voids were explicitly considered, the effect of void location in the microstructure was not analyzed and the HMX material did not contain a polymer binder typical of polymer-bonded explosives (PBX). It is acknowledged and understandable that such millimeter-scale explicit 3D mesoscale models do not necessarily match the spatial resolutions of mesoscale models with overall sizes on the order of microns or hundreds of microns. Further, the void sizes considered are relatively large among those in all studies involving voids. Still, Miller et al. [38] have shown that the models and approach allow new issues to be studied and trends to be delineated.

In this paper, we use this approach to study the unexplored effects of void location and quantify how the SDT behavior and the Pop plot of a polymer-bonded explosive (PBX) evolves as void populations are placed in different constituents of the PBX microstructure. To this effect, randomized distributions of voids are introduced to form four separate material cases: (1) voids only in the binder, (2) voids only in the grains, (3) voids in both the grains and binder, and (4) no voids in the microstructure. Each material case is subjected to shock loading and the SDT behavior is analyzed. We note that while it is currently difficult to experimentally control the exact positions of voids in a PBX, simulations can be used to systematically delineate the effects of void distributions in the grains and binder. This can deepen understanding of the mechanisms governing SDT and lead to tailoring of material properties and identification of routes to improve material properties. In this endeavor, we probe the dependence of detonation behavior on the relative location of the voids using the previously stated fully microstructure-explicit and void-explicit model framework. The quantity of interest (QoI) is the run-to-detonation distance (RDD) as it relates to the porosity distributions. We structure the computations to also obtain probabilistic representations for the detonation sensitivity and study the effects of void distribution on detonation. To this end, statistically equivalent microstructure sample sets (SEMSS) are generated and used, leading to the probabilistic formulations for the RDD as a function of shock pressure. Under the current setting of a PBX with different distributions of voids, these relations are expressed in forms that allow important questions to be answered, such as (a) what is the probability for observing SDT by any given run distance and under any given shock pressure? (b) what is the minimum run distance required for achieving SDT with a required level of probabilistic confidence using a given shock pressure? (c) what is the minimum shock pressure required to achieve SDT by a given run distance with a prescribed level of probabilistic confidence? This type of

probabilistic analysis is useful for quantifying the influence of specific microstructural attributes on PBX ignition sensitivity in both the idealized microstructures presented here and more realistic microstructures in the future.

Framework of Analysis

To accurately model the SDT behavior in a PBX, a model must have sufficiently resolved microstructure heterogeneities where hot spots can form, as well as a calibrated chemical kinetics model, an equation of state (EOS) and constitutive laws to describe the phase change of the energetic material. The model should also be sufficiently large to capture the complete length scale of the impact, wave propagation, reaction initiation and growth, SDT, and post SDT detonation propagation. This necessitates an overall model size on the order of millimeters, as the run distance of materials is typically several mm. To this end, the fully three-dimensional (3D) framework of Miller et al. [38] is adopted. The 3D simulations are performed using CTH [39], a solid mechanics code created by Sandia National Laboratory. Sustained shock loading is imparted on the sample by a thick aluminum flyer, with flyer velocities ranging from 800 m/s to 1500 m/s. The loading results in shock pressures between 3 and 8 GPa in the material. The method of microstructure development is explained in Section 2.1, the constitutive models used are summarized in Section 2.2, and the effects of mesh resolution are explored in Section 2.3.

2.1. Material, Model, and Microstructure

The material setting for this study is a PBX consisting of PETN high explosive crystal grains and a HTPB polymer binder. PETN has seen wide use in applications for decades [40]. HTPB is a polymer binder commonly used in energetic material applications such as solid rocket motor propellants [41]. This combination of constituents is chosen here in part because of readily available Arrhenius Reactive Burn (ARB) model parameters that are calibrated to experimental data [42].

To generate the microstructures for the PBX with PETN grains in a HTPB binder, a large size fully dense polycrystal PETN is first created by Voronoi tessellation. The size of this large "ingot" is 3×3×15 mm. The process involves first seeding the space with ~38,000 randomly placed points which serve as nucleation sites of individual crystallites (grains). The average grain equivalent sphere diameter is determined by the number of the starting seeds. The Voronoi tessellation algorithm yields the final polycrystal microstructure that is the end result of random outward growth in all directions of the crystallites from the seed locations until neighboring crystallites meet to form planar boundaries which are the grain boundaries in the microstructure. To obtain the space occupied by the polymer binder, each grain boundary is separated into two identical planar facets, one for each of the contacting pair of grains. All the grain boundary facets are shrunk inward toward the centroids of their respective grains by amounts that are randomized within prescribed limits, until the total grain volume fraction reaches 75% (the binder volume fraction reaches 25%). All facets maintain their orientations during the shrinking process to ensure affinity of the grains to their original shape in the fully packed polycrystal. This process of composite microstructure generation allows any high grain volume fractions to be reached. In contrast, the method of microstructure composition developed by Wei et al. [43] can reach a maximum grain volume fraction of ~80%.

To emulate the cutting of multiple smaller statistically similar samples from the same bulk ingot in experiments, multiple microstructure samples (five in this paper) with an overall size of 1×1×5 mm are cut from this computationally generated "ingot". These five microstructures (shown in Fig. 1(a)) are taken as the Statistically Equivalent Microstructure Sample Set (SEMSS) used in the analyses to be carried out. The grains in the SEMSS have a mean equivalent sphere diameter of 150.2 μm and conform to the size distribution shown in Fig. 1(c). This size distribution roughly matches those seen in PBX 9501 as reported by Skidmore et al. [44]. Although PBX 9501 is comprised of HMX (not PETN) grains, this size distribution emulates a realistic material setting.

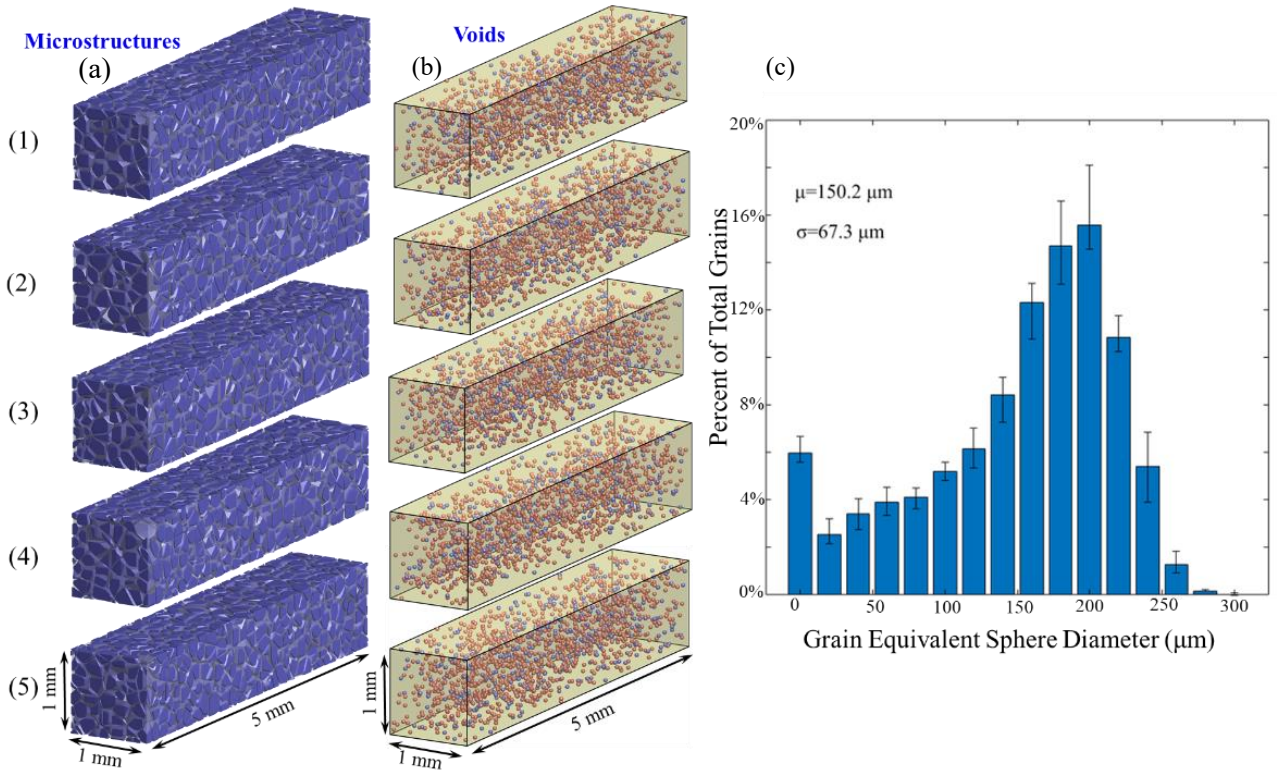

Fig. 1 - (a) Statistically equivalent microstructure sample set (SEMSS) with five samples each 1×1×5 mm in size, with the PETN grains shown in dark blue and the HTPB polymer matrix shown in light gray. (b) The corresponding fields of randomly placed spherical voids (50 μm in diameter) for the samples in (a), only 20% of all the voids are shown for visual clarity. The voids in the grains are red and the voids in the polymer are dark blue. (c) The grain size distribution for the samples in (a). The error bars denote the range of variations among the multiple samples in (a).

A population of identical spherical voids 50 μm in diameter are randomly introduced to the samples in Fig. 1(a). For visual clarity, the voids fields for the samples are shown separately in Fig. 1(b). The voids located in the grains are colored red and the voids located in the polymer are colored blue. The voids in each sample are allowed to overlap to create more heterogeneous void fields. The total number of voids for each sample ranges from ~7,700 to ~8,000 (accounting for overlap), resulting in a total porosity of 10%. These void fields are utilized to create the four material cases we investigate: (1) No Voids (NV), (2) Voids in Grains (VG), (3) Voids in Binder (VB), and (4) Voids in both Grains and Binder (VG+B). The NV case uses the SEMSS in Fig. 1(a) without any voids. In the VG case, only voids in the grains (red) in Fig. 1(b) are used, if a void overlaps with both grain and binder material in this case, only the part of the void in the grain is allowed. Since the voids account for 10% of the total sample volume and the grains constitute 75% of that volume, the total porosity of the VG case on average is 7.5%. Similarly, the VB case is created by using voids in Fig. 1(b) (blue) that are exclusively in the binder. Since the binder represents 25% of the microstructure volume, the total porosity for the VB case on average is 2.5%. In the VG+B case, all voids in both the grains and binder in Fig. 1(b) are permitted, this case has a porosity of 10%. Taken together, the four cases allow us to assess (i) how voids affect the behavior of the PBX, and (ii) what the relative contributions of the voids in the grains and the voids in the binder are to that overall effect.

In reality, PBX have heterogeneous microstructural features much smaller than those discussed above. Examples include sub-micron voids and microcracks. Willey et al. measured the distribution of void diameters in both LX-10 and PBX 9501 at room temperature using USAXS and observed most voids were smaller than 5 μm [25]. Such features are computationally expensive to model at the overall sample size scale of this paper and are therefore not resolved

here. We note that they have been analyzed previously using different model settings [7, 9-11, 29, 43, 45, 46]. The void diameter chosen for this study is relatively large. It is necessitated by computational cost. However, the framework allows the effects of voids and behavior trends to be explored. In particular, it provides a setting for assessing how biasing PBX microstructures with voids located in different constituents can be a means for tuning the sensitivity of high explosives.

2.2. Configuration of analyses

Loading is in the form of impact along the longitudinal axis of the samples by a thick aluminum flyer at a velocity of U_P. This imparts a sustained shock loading on the sample without the effect of shock release for the duration of analyses. The sides (lateral surfaces) are constrained in a frictionless manner to ensure planar, macroscale sample level uniaxial strain shock loading to mimic planar impact experiments. More details can be found in Miller et al. [38].

2.3. Constitutive Relations

An elastic-perfectly plastic flow stress model based on the von Mises yield surface concept (EPPVM) is employed to account for the plastic deformation of the PETN grains. This model accounts for thermal softening and density degradation of the material under shock loading. The parameters of the EPPVM model for PETN grains are shown in Table I, and are taken from [47].

Table I. PETN material parameters for EPPVM

ρ_0	σ_y	ν	T_{melt}
1.774 g/cm^3	0.26 GPa	0.3	414.4 K

In the table, ρ_0 is the reference density, σ_y is the yield stress, ν is the Poisson's ratio, and T_{melt} is the melting temperature of PETN in Kelvin.

The yield surface is given by

$$Y = \begin{cases} \sigma_y, & \text{if } T < T_{melt}; \\ \dfrac{(T - T_{melt})(\alpha - 1)}{T_{melt}} \sigma_y, & \text{if } T \geq T_{melti}. \end{cases} \quad (1)$$

In the above expressions, Y is the current flow stress or yield strength of the material, T is the temperature and α is equal to ρ_0/ρ, with ρ being the current density. If the second invariant of the stress deviator tensor (J_2) is larger than the current yield strength represented by the yield surface, then all deviators are multiplied by

$$s = s * Y / J_2, \quad (2)$$

where s is the stress deviator, and J_2 is the second invariant of the stress deviator tensor.

A first order Mie Grüneisen Equation of State (MGEOS) is used to describe the bulk response of PETN grains to hydrostatic pressure in the unreacted solid phase, i.e.,

$$p = \frac{p_0 C_0^2 \left(1-\frac{\rho_0}{\rho}\right)\left[1-\frac{\Gamma_0}{2}\left(1-\frac{\rho_0}{\rho}\right)\right]}{\left[1-s\left(1-\frac{\rho_0}{\rho}\right)\right]^2} + \Gamma_0 E. \tag{3}$$

Here, p is pressure, ρ_0 is the reference density of PETN, ρ is the current density of PETN, Γ_0 is the Grüneisen parameter, C_0 is the bulk sound speed, and s is the slope of the Hugoniot. E is the internal energy per unit volume which can be determined by integrating the specific heat with respect to temperature at constant volume, i.e.,

$$E = \frac{1}{V_0}\int_0^T c_v dT. \tag{4}$$

The parameters for the MGEOS used for PETN can be found in the CTH EOS package [48]. The PETN reaction product EOS is described by tabular data in the form of a SESAME table [48].

2.3 Chemical Kinetics Model

The chemical reaction can be phenomenologically modeled by an Arrhenius-type kinetics model [12] calibrated to experimental data [13, 49], data from Density Functional Theory/chemical kinetics calculations [50, 51], and/or the results of molecular dynamics simulations [52]. There is often a tradeoff between model accuracy and simulation runtime. To minimize this computational cost, calibrated empirical reactive burn models are often used to simulate the evolution of chemistry without needing to explicitly model chemical species. Miller et al. [53] used a history variable reactive burn (HVRB) model to capture a mixture of homogeneous and heterogeneous detonation behavior in pressed HMX. Another popular model is the ignition and growth (I&G) model proposed by Lee and Tarver in 1980 [54]. This model treats the initial hot spot chemistry (ignition) and subsequent evolution (growth) independently and has been used to successfully model shock initiation and detonation [10, 54, 55].

In this work, the Arrhenius Reactive Burn chemical kinetics model (ARB) is used to track the rate of chemical reaction in the PETN grains. This empirical model more accurately tracks the development of local field variables, such as temperature and pressure rise due to chemical reaction, than other burn models, such as History Variable Reactive Burn (HVRB) [53]. The ARB model tracks the rate of chemical reaction in the PETN using the form

$$d\lambda/dt = \begin{cases} (1-\lambda) F \exp(-\Theta/T), & \text{if } T \geq T_i; \\ 0, & \text{if } T < T_i. \end{cases}, \quad \text{with } \Theta = \Theta_0(1 + A_P P). \tag{5}$$

In the above relations, λ is the fraction of reacted material, t is time, T is temperature in Kelvin, F is a pre-exponential factor, Θ_0 is the activation temperature of the material, A_P is a parameter quantifying the pressure dependence of the reaction rate, and P is pressure. T_i indicates the threshold temperature below which the reaction rate is zero. The parameters for the ARB model are taken from the CTH ARB reference manual. Parameter tuning methods can be found in [42].

2.4 Mesh Convergence Study

A mesh convergence study is performed using RDDs and initial shock pressure as the measures of focus. This is to ensure that the mesh is sufficiently fine to sufficiently capture the heterogeneities in the microstructures and the

physical fields so as to lead to sufficiently predict these macroscopic quantities which are the key QoIs in this study, as opposed to minute details of the local field quantities such as temperature or pressure, as is the case in other studies. Among the four materials cases here, the VG+B case has the most stringent mesh resolution requirement as it is the one with the largest amount of microstructural heterogeneity. Therefore, it is used in the convergence study. The result shows that mesh elements smaller than 10 μm yield negligible changes in the RDD. This is consistent with the finding of Miller et al. [53] who conducted such a mesh convergence study of initial shock pressure as well as RDD in granular HMX with varying degrees of microstructural heterogeneity, including HMX grains and 50 μm diameter voids (the same in the current analyses). Their result showed that mesh refinement to element sizes below 10 μm yields no noticeable difference in either the shock pressure or the RDD. Based on these analyses, an element size of 10 μm is chosen in our simulations. This choice provides a balance between computational cost and the need to sufficiently resolve the macroscopic properties of interest which are the focus of this study, not details of local fields.

Results and Discussion

In this section, we present the results of our three-dimensional SDT modeling effort. Section 3.1 discusses how the RDD is measured during each simulation. Section 3.2 compiles the RDD data into Pop plots for each material case. Finally, Section 3.3 provides a probabilistic analysis for interpreting these results.

3.1 Shock to Detonation Transition Process

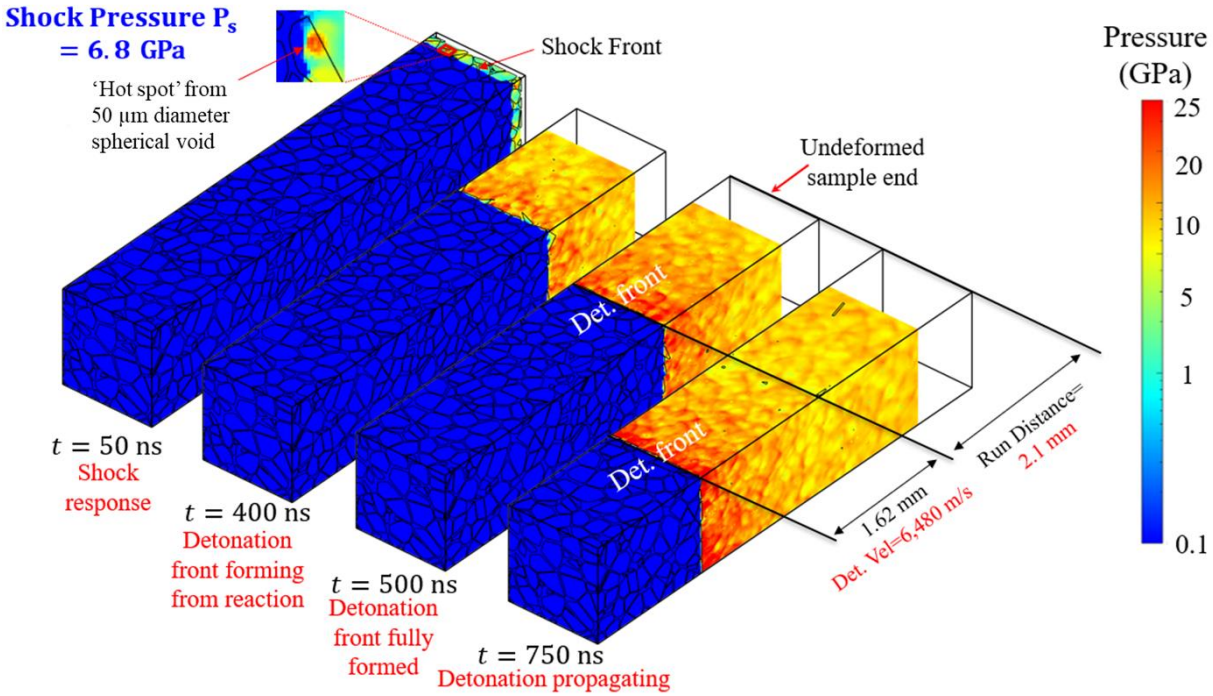

Fig. 2 – The shock-to-detonation transition process in PETN/HTPB PBX for one of the samples in the SEMSS with voids in both grains and binder. Time from the onset of shock loading is shown.

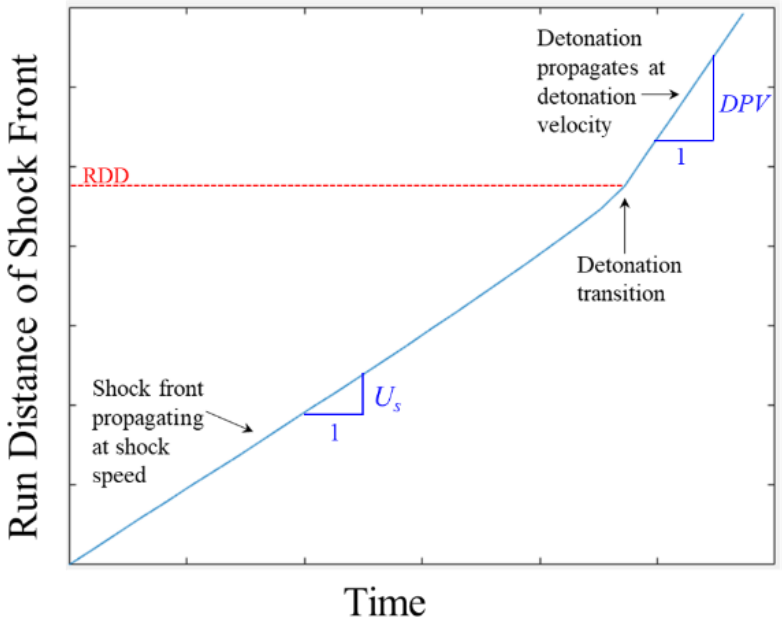

Fig. 3 – Position of shock/detonation front as a function of time. The slope of this relation indicates the shock velocity and the detonation propagation velocity (DPV). The transition of the slope indicates SDT and the RDD.

As energy dissipates in the material, hot spots can ignite and jump start the chemical reaction in the HE granules [9, 56, 57]. As the chemical reaction evolves, phase changes lead to rapid increases in the temperature and pressure of the material, which may send secondary shock waves into adjacent material, igniting additional hot spots [58]. If an insufficient hot spot density is present to propagate the reaction, the hot spots are located in constituents with less dissipation or less chemical energy, or the shock duration was insufficient, the sample may be quenched due to the rarefaction wave [59]. If a sufficient quantity of hot spots react in close proximity, the energy dissipation due to chemical reaction can lead to a cascading effect of hot spot ignition, forming a detonation front behind the initial shock wave. This detonation front is self-sustaining and quickly overtakes the shock front, transitioning the shock wave into a detonation wave [2, 29, 60]. This process by which the self-sustaining detonation wave catches up and ultimately overtakes the incident shock front is known as the shock to detonation transition point. The whole process of shock wave propagation, hot spot formation, ignition, reaction propagation, transition from shock to detonation, and detonation propagation in un-disturbed material is captured, as shown in Fig. 2. The distance the shock wave front travels before being overtaken by the detonation wave front is the run distance to detonation or run-to-detonation distance (RDD) and is a common metric used in the form of a Pop plot [61] to gauge the detonation sensitivity of an HE.

Materials with longer RDDs for a prescribed shock pressure are considered to have a lower shock initiation sensitivity. Since the detonation front forms so close to the shock front in heterogeneous detonation events, it may be difficult to precisely determine when the detonation front has fully formed. The method we use to determine when the sample has transitioned from shock to detonation is the same method used by Miller et al. [11]. It involves measuring the position of the shock front as a function of time. This measurement is made throughout the entire process, as shown in Fig. 3. Initially, the incident mechanical shock wave travels at a constant velocity U_s through the sample. As the detonation wave forms following the SDT, the shock front evolves into the detonation front and accelerates to the detonation velocity, as indicated by a steeper slope in Fig. 3. This point of sharp change in the velocity of the shock front is where the RDD is measured.

3.2 Characterization of the RDD

The primary QoI in the analyses of the sensitivity of energetic materials is the Pop plot, or the relation between the RDD and the shock input pressure. This relation quantifies the distance a shock wave must propagate through a material until the detonation front fully forms under a given shock pressure. Pop plots allows the sensitivities of different materials to be compared. Here, a systematic quantification of the relation between the RDD and shock pressure is performed.

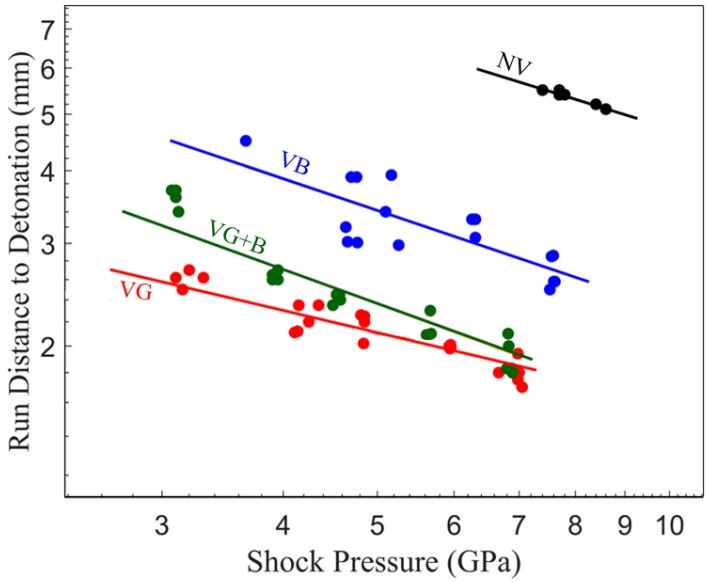

Fig. 4 – Run distance to detonation as a function of shock pressure for the four material cases analyzed: no voids (black), voids in binder (blue), voids in grains (red), and voids in both grains and binder (green). Solid lines represent fits of the data to the power law relation in eqn. (6).

Table II. Effect of void placement on RDD

SEMSS	Average Decrease in RDD relative to No Voids case
Voids in Binder	52.7%
Voids in Binder and Grains	64.8%
Voids in Grains	70.2%

Figure 4 shows the Pop plot with the RDD values obtained from the simulations. Each data point represents one sample in the corresponding SEMSS. The data set for each material case is fitted to the power law relation

$$(x^* - x_0^*) = H(P_s - P_0)^{-m} \tag{6}$$

in which x^* is the run distance at shock pressure P_s, H is a material-dependent scaling parameter, and x_0^* and P_0 are the minimum RDD and shock pressure for observing SDT, respectively, and m is an exponential material constant. This equation, first used by Miller et al. [38], is a generalized version of the relation previously used (see, e.g., [11]). The values of parameters H and m are listed in Table III. x_0^* and P_0 are insensitive parameters whose choices are discussed in [38].

The lines in Fig. 4 are fits of the data sets to eqn. (6) and represent the conditions associated with a 50% probability of SDT for the four material cases. More discussions of the lines will be given later in Section 3.3. The sensitivity of energetic materials to initiation and detonation can be gauged from these lines. The height of a line is analogous to the overall sensitivity of a material, while the slope of a line indicates the pressure-dependence of a material's sensitivity. Higher RDDs under a given shock pressure lower sensitivity to impact. In Fig. 4, the NV case has the highest RDDs, followed by the VB, VG+B, and VG cases, in that order. This trend is expected, as voids provide the additional heterogeneities beyond the grain and binder microstructure morphology for hot spot formation. The lines for the cases serve as an average means of comparison for the relative sensitivities among the cases. Table II shows the average decrease in RDD values relative to the NV case for the other three material cases. It is apparent that a small number of voids can cause the RDD values to drastically decrease. For example, the VB case has only a porosity level of 2.5% by volume due to voids in the binder but has RDDs that are 52.7% lower on average relative to the NV case. The VG case has a porosity of 7.5% by volume due to voids in the grains and has RDDs that are 70.2% lower on average relative to the NV case. This indicates that the voids in the grains play a more significant role in the formation of hot spots that lead to reaction and SDT compared with voids in binder. This is logical, as the grains are the primary reactive material in the microstructure. What stands out as interesting is the observation that the VG+B case, despite having the combined voids of the VB and VG cases (i.e., 2.5% voids in the binder and 7.5% voids in the grains, for a total porosity of 10% by volume), has an average RDD decrease from the NV case of only 64.8%, less than that of the VG case. This trend of "1+1 < 1" or "combining two populations of voids leads to RDDs that are lower than the RDDs of the material with only voids in grains is quite counterintuitive. Yet, it can be explained as follows using the images in Fig. 5. Relative to the VG case, when voids are further introduced in the binder, the material attains an overall higher level of porosity which leads to lower pressures in the microstructure in the early part of the response following the onset of loading. The lower pressures slow the development of hot spots relative to that in the VG case, see Fig. 5 (a, d). Thus, the entire process of hot spot evolution is delayed (compare Fig. 5(b, c) and (e, f)), resulting in longer RDDs. In contrast, at pressures above ~7 GPa, the VG+B and the VG data sets converge in Fig. 4. The convergence in behavior is due to the fact that the development of hot spots is nearly identical in these two cases, as shown in Fig. 6. This trend suggests that, at lower shock pressures, the effects of microstructure and voids cause the behavior of materials to be different or distinguishable; but at high shock pressures, loading-induced effects appear to dominate, and the effects of material heterogeneities are masked and manifest to a much lesser degree. To fully confirm this effect, test cases of samples subjected to shock loadings of greater than 7 GPa are required to observe whether the Pop plot lines fully converge. This observation is consistent with the analyses of Wei et al. [43] and experimental observations made by Borne [62]. Note that the porosity levels analyzed here are similar to the ~1-10% porosity levels reported for the materials in experiments [63].

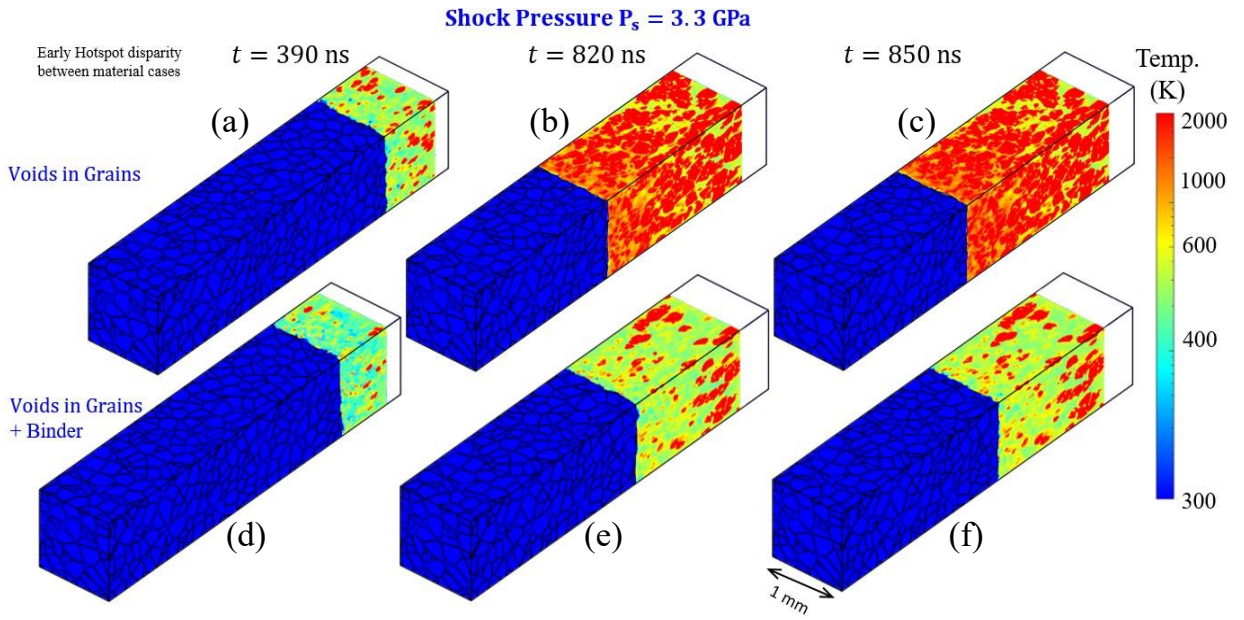

Fig. 5 – The development of hotspot in early stages following onset of loading in the VG material case (top row, a-c) and the VG+B material case (bottom row, d-f) under a relatively low shock pressure of P_s = 3.3 GPa. The VG+B case has more voids, but delayed hotspot development.

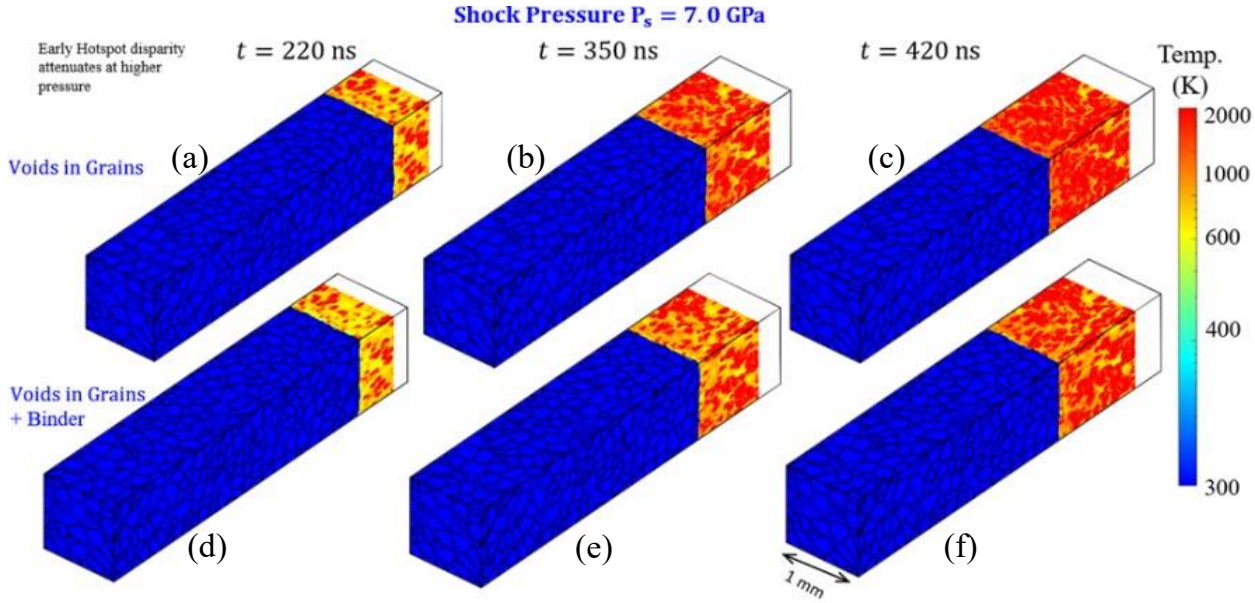

Fig. 6 – The development of hotspot in early stages following onset of loading in the VG material case (top row, a-c) and the VG+B material case (bottom row, d-f) under a relatively high shock pressure of P_s = 7.0 GPa. The VG+B case has more voids but essentially the same rate of hot spot development.

The rank order of the heights of the Pop plot lines, as well as the slopes of the lines, are two key metrics for evaluating the shock initiation sensitivity of materials. The formation of the detonation front is intimately tied to the levels of heterogeneity in the energetic composite. As shown in Fig. 5, voids in the grains play a more dominant role in determining the sensitivity than voids in the binder. As long as voids are present in the grains, further addition of voids to the binder may not significantly increase the sensitivity and may in fact decrease the sensitivity by weakening the shock loading or dissipating early detonation front energy via collapsing of the voids in the binder which is either inert or weakly exothermic by releasing less than a hundredth of the heat of PETN on a unit weight basis [64].

3.3 Quantification of Uncertainty in RDD

Due to the strong dependence of ignition response on microstructure and voids whose heterogeneities are intrinsically stochastic, variations in the microstructure and void distribution result in statistical data scatter in the Pop plot, giving rise to uncertainties in the assessment of the macroscopic material behavior. Wei et al. [43] and Miller et al. [53] pioneered a probabilistic approach to quantify this uncertainty, thereby allowing deeper understanding of the interplays among material response, microstructure, voids, and loading conditions. Here, we use their approach to quantify the uncertainties in the RDD as a function of loading. In doing so, we use the relation to quantify the loading (shock pressure) required to ensure SDT within a given run distance with any level of prescribed probability. Additionally, the relation is also used to specify the minimum run distance needed to achieve full SDT with a desired level of probability. These analyses have applications in the design of devices and choice of HEs for different applications.

Equation (6) and its geometric representations in Fig. 4 embody the macroscopic conditions (RDD-shock pressure combinations) corresponding to a 50% probability of observing SDT. Parallel shifts of the 50-50% lines lead to lines for conditions corresponding other levels of probability between 0 and 1 of SDT in the RDD-shock pressure space (Pop plot space). To facilitate the analysis and quantification, a non-dimensional parameter

$$D = \frac{\left(P_s - P_0\right)^m \left(x^* - x_0^*\right)}{H} \tag{7}$$

can be introduced [11, 43], where $0 \le D < \infty$. The parameters in eqn. (7) are the same as those used in eqn. (6). When D is equal to 1, the relation in eqn. (6) and the lines in Fig. 4 for a 50% probability of SDT are recovered. $D > 1$ and $D < 1$ correspond to conditions for observing SDT at greater than 50% and less than 50% probabilities, respectively. A value of D is calculated for each data point in Fig. 4. For each material case, the probability $\mathcal{P}$ of observing SDT at a particular D value is equal to the fraction of the total number of data points in Fig. 4 in that data set that are below the line represented by eqn. (7). Alternatively, $\mathcal{P}(D)$ is equal to the fraction of the number of data points in each data set that are to the left of D in Fig. 7. Note that Fig. 7 uses ln(D) in the abscissa, each data set is fitted to a log-normal cumulative distribution function (CDF) of the form

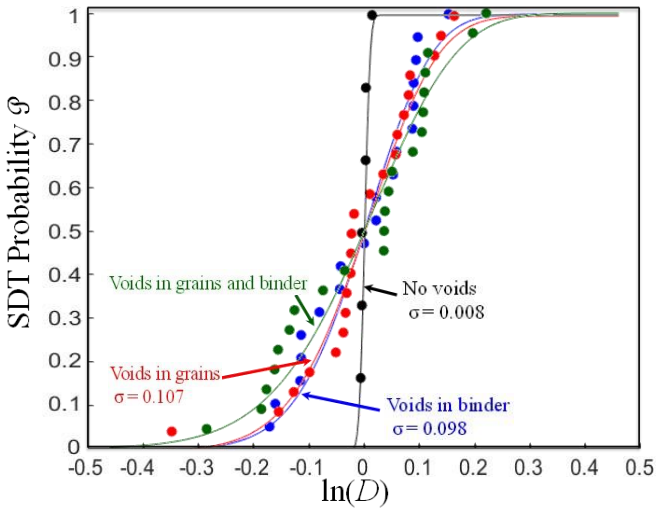

Fig. 7 – Log-normal cumulative SDT probability of the four material cases.

$$\begin{aligned}\mathscr{P}(P_s, x^*) &= \frac{1}{2} + \frac{1}{2}\,\mathrm{erf}\left[\frac{1}{\sqrt{2}\sigma_d}\left(\ln D\right)\right] \\ &= \frac{1}{2} + \frac{1}{2}\,\mathrm{erf}\left[\frac{1}{\sqrt{2}\sigma_d}\left(\ln\left(\left(P_s - P_0\right)^m\right) + \ln\left(x^* - x_0^*\right) - \ln H\right)\right].\end{aligned} \tag{8}$$

Where, σ_d is the standard deviation of the normal distribution and use has been made of eqn. (7). This relation allows the probability of observing SDT at any point in the Pop plot space (Fig. 4) to be evaluated, see Wei et al. [43] and Miller et al. [53]. Note that $\mathscr{P}(P_s, x^*)$ is the probability of observing SDT at any RDD up to x^* (as opposed to at x^*) under input shock pressure P_s. The values of the material parameters in eqn. (8) are shown in Table III.

Table III. Pop plot Material Parameters for eqn. (8)

Sample	H (GPa^m·mm)	m
No Voids	14.977	0.507
Voids in Binder	8.292	0.599
Voids in Grains	2.871	0.178
Voids in Binder and Grains	6.858	0.741

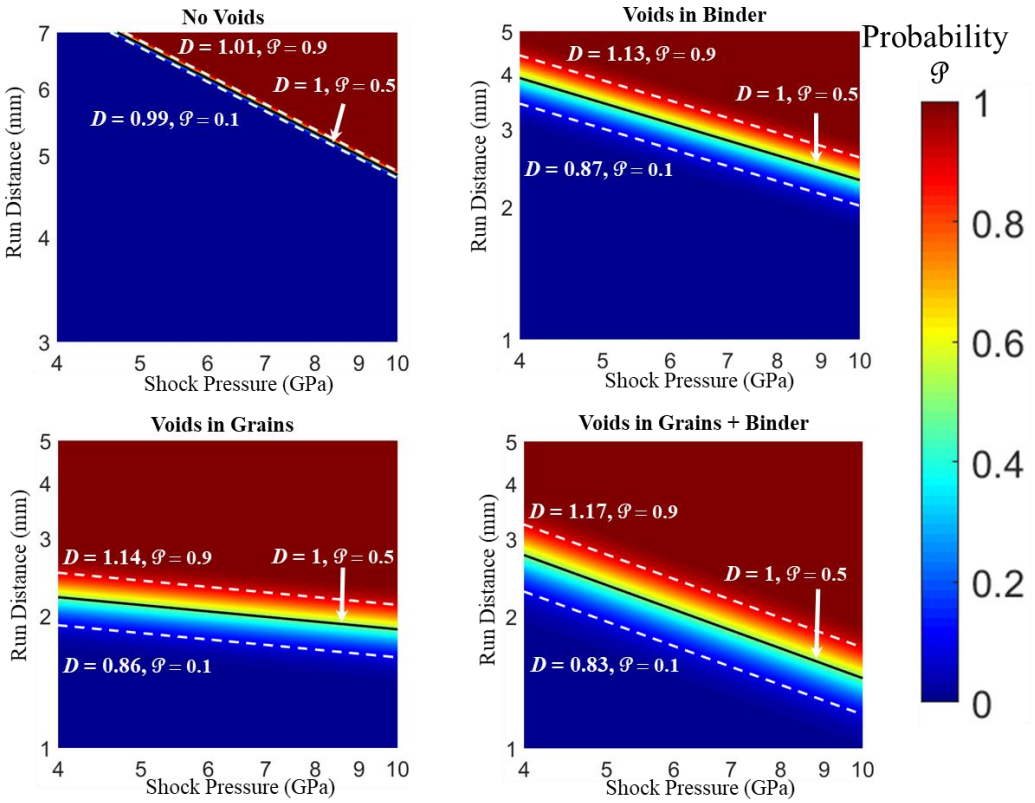

Fig. 8 – Cumulative SDT probability maps for the four material cases. D = 1 corresponds to the line for conditions for a 50% probability.

Equation (8) is evaluated over a range of run distances and shock pressures to generate the probability map for each material case shown in Fig. 8. The black line is the line for a 50% probability. This line corresponds to the threshold by which half of the samples tested will have RDDs above it, and half will be below. The lower and upper white dashed lines represent SDT probabilities of 10% and 90%, respectively. The 90% probability line is the line below which 90% of samples in a set will have reached SDT. Similarly, the 10% probability line is the line below which 10% of the samples in the set will have reached detonation.

These probability maps and the relation in eqn. (8) can be recast in alternate forms to answer other questions about uncertainties of the quantities of interest as they relate to one another. Two alternative forms, one shown in Fig. 9 and eqn. (9) and the other in Fig. 10 and eqn. (10), express shock pressure as a function of run distance and probability and the run distance as a function of shock pressure and probability, respectively. These maps allow for new interpretations of the Pop plot data. For example, to ensure SDT by a given RDD with a desired probability, Fig. 9 and eqn. (9) can be used to obtain the necessary input shock pressure. On the other hand, to ensure a desired probability of SDT at a given input shock pressure, Fig. 10 and eqn. (10) can be used find the minimum run distance required. Equations (9) and (10) are used to generate Figs. 9 and 10 respectively, see Miller et al. [53].

$$P_s(\mathscr{P}, x^*) = \left\{ \frac{H}{\left(x^* - x_0^*\right)} \exp\left[\sqrt{2}\sigma_d \left(\text{erf}^{-1}\left(2\mathscr{P} - 1\right)\right)\right] \right\}^{1/m} + P_0, \tag{9}$$

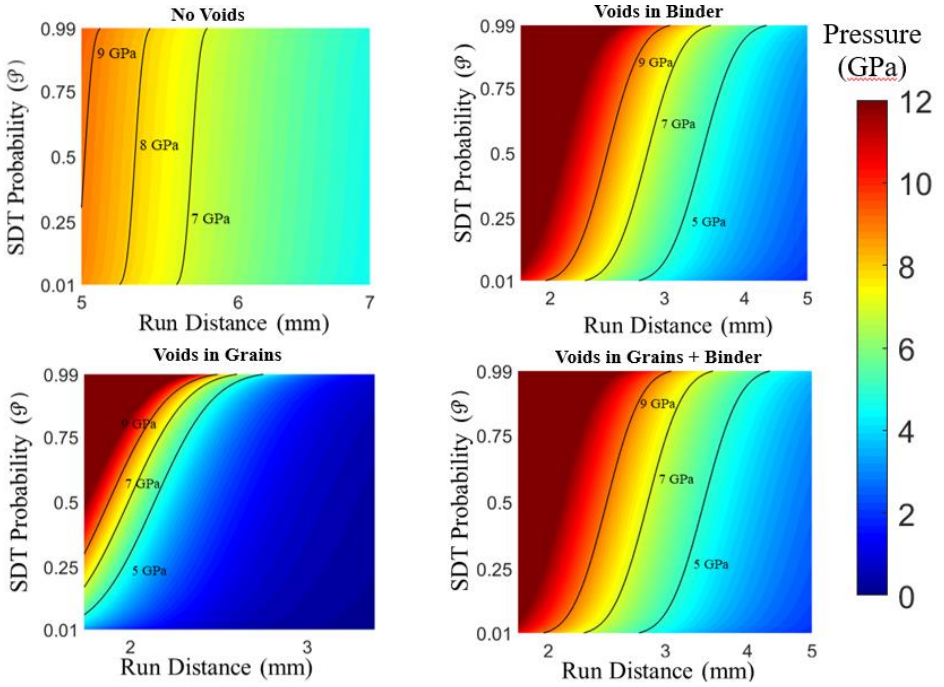

Fig. 9 – Minimum shock pressure needed to achieve SDT by a given run distance with a desired probability.

$$x^*(\mathscr{P}, P_s) = \frac{H}{\left(P_s - P_0\right)^m} \exp\left[\sqrt{2}\sigma_d \left(\text{erf}^{-1}\left(2\mathscr{P} - 1\right)\right)\right] + x_0^*. \tag{10}$$

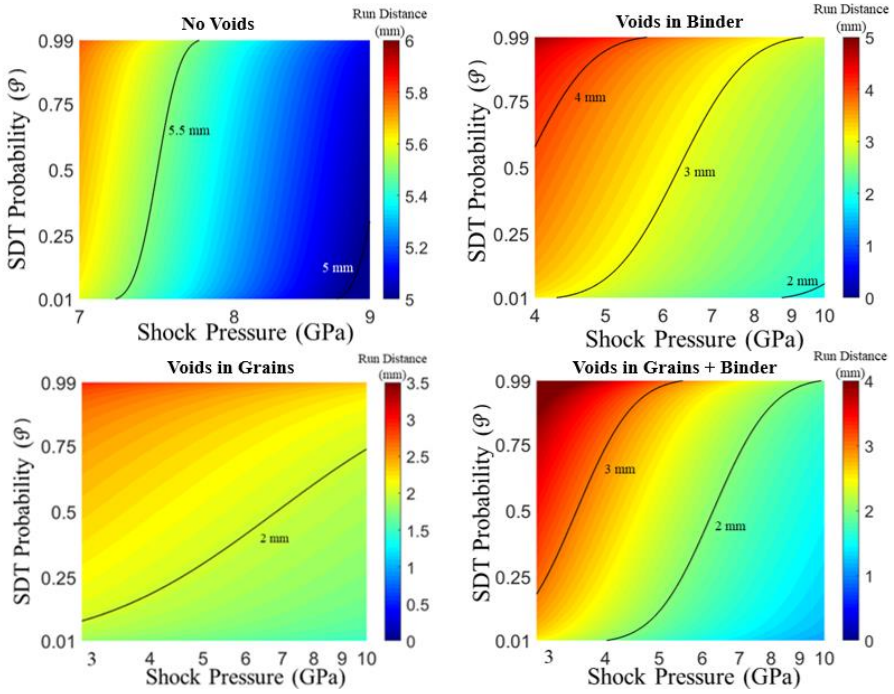

Fig. 10 – Minimum run distance needed to achieve SDT with a prescribed level of probability under a given input shock pressure.

The above equations and maps allow the probabilistic Pop plot of a material to be used to not only assess the sensitivity with uncertainty quantification, but also answer design and risk evaluation questions such as (a) what is the probability for observing SDT by a given run distance and under any given shock pressure? (b) what is the minimum run distance required for achieving SDT with a required level of probabilistic confidence using a given shock pressure? (c) what is the minimum shock pressure required to achieve SDT by a given run distance with a prescribed level of probabilistic confidence? Such questions are of importance in a range of applications. For example, an engineer may be designing a compact detonator that has strict requirements on maximum length of the component. This length dictates that SDT must occur within a certain run distance. To ensure SDT at a prescribed confidence level, Fig. 9 and eqn. (9) allow the minimum operating input shock pressure that must be applied.

Conclusion and comment

The effects of void location relative to constituents in the microstructure on the behavior of energetic materials have previously not been studied using microstructure-explicit, millimeter-scale, three-dimensional simulations. In this paper, a systematic study has been carried out. The approach uses fully three-dimensional simulations of the shock to detonation process in a porous PBX comprising of 25% HTPB binder and 75% PETN high explosive crystal grains are performed. The model explicitly resolves the microstructure and the void population in the designed material. The analyses focus on the prediction of the shock to detonation transition (SDT) threshold (Pop plot) under monotonic loading conditions. In particular, the effects of the distribution of the void population in the microstructure (i.e., how the voids are located relative to the polymer binder and the grains) are systematically delineated by using four material cases: microstructures without voids (NV), microstructures with voids only in the grains (VG), microstructures with voids only in the binder (VB), and microstructures with voids in both grains and binder (VG+B). The effects on the detonation sensitivity (Pop plot) are ranked-ordered. The results show trends that are consistent with the generally accepted understanding of the effect of microstructure heterogeneity on detonation sensitivity.

Within the microstructure setting, voids distribution or positioning relative to the grains and the binder have a profound influence on the SDT behavior. Specifically, the case without voids has significantly lower sensitivity (higher run distances) than the cases with voids. Adding voids only in the binder lowers the average RDD values by 52.7% relative to the no voids (NV) case. Voids in the grains only case (VG) has significantly higher sensitivity (or lower average RDD) than the NV case, with average the run distance 70.2% lower relative to the NV case. The case with voids in both grains and binder (VG+B) has average RDD values 64.8% lower than those of the case without voids (NV), suggesting more voids does not necessarily lead to lower RDD under any circumstance, especially if the additional voids are in the binder. Further, the effect of the additional voids in the binder tends to disappear relative to the VG case as the shock pressure approaches levels above ~6-7 GPa. RDDs for this case approach the values of the voids in grains only case (VG) at higher shock pressures, implying that the influence of void location on likelihood observing of initiation becomes less pronounced at higher shock pressures.

Probabilistic quantifications in the forms of both analytical relations and graphical maps of the run distance to detonation (RDD) for all the material cases have been developed. These relations and maps provide new tools for understanding the probabilistic nature of the initiation behavior of high explosives and the associated uncertainties. In particular, they allow important questions to be answered, including (a) what is the probability for observing SDT by any given run distance and under a given shock pressure? (b) what is the minimum run distance required for achieving SDT with a required level of probabilistic confidence using a given shock pressure? (c) what is the minimum shock pressure required to achieve SDT by a given run distance with a prescribed level of probabilistic confidence? The trends and relations obtained can be used in developing concepts for sensitizing or desensitizing PBX as well as understanding the differences in the behavior of different batches of the same PBX. Although the current processing and synthesis techniques do not permit direct control of the locations of voids in microstructures of energetic materials,

emerging or future processing and fabrication techniques such as additive or subtractive manufacturing may allow direct placement of voids or biasing voids toward parts of a microstructure.

It is again acknowledged that the void size considered here is relatively large among void sizes considered in mesoscale simulations. This reflects a limitation of the extremely high level of computational resources demanded by the fully 3D models and the explicit resolution of both microstructure and voids pursued. However, the models allowed underlying trends to be delineated. As more advanced computational resources become available in the future and algorithms are improved, better resolutions and smaller void sizes can be considered within this approach. Additionally, future iterations of this methodology should consider incorporating entire void distributions to more accurately represent experimental microstructures. It is also acknowledged that how voids exclusively located along the grain-polymer binder boundaries affect the behavior of PBX has not been studied here. This can be the topic of a future analysis.

Acknowledgements

This research is supported by the Defense Threat Reduction Agency (DTRA) through grant HDTRA1-18-1-0004 to Georgia Tech (Dr. Jeffery Davis). CC is supported by Los Alamos National Lab (LANL) via contract 727563 during the last stage of the preparation of this publication. CM's contribution to this work was performed under the auspices of the U.S. Department of Energy by Lawrence Livermore National Laboratory under contract DE-AC52-07NA27344. Lawrence Livermore National Security, LLC. LLNL-JRNL-818186. Calculations are carried out on supercomputers at the ARL DSRC through the US DoD HPCMP. We would like to thank Dr. David Kittell for helpful insight into CTH and the models used. Thanks are also extended to Dr. Yaochi Wei for assistance in our modification of the internal GT codes used for the microstructure and graphics generation.

Data Sharing Policy

The data that support the findings of this study are available from the corresponding author upon reasonable request.

REFERENCES

1. Bowden, F.P., Yoffe, A.D., and Hudson, G.E., *Initiation and Growth of Explosion in Liquids and Solids.* American journal of physics, 1952. **20**(4): p. 250-251.
2. Wood, M.A., Cherukara, M.J., Kober, E.M., Strachan, A., *Ultrafast Chemistry under Nonequilibrium Conditions and the Shock to Deflagration Transition at the Nanoscale.* Journal of Physical Chemistry C, 2015. **119**(38): p. 22008-22015.
3. Campbell, A.W., W.C. Davis, and J.R. Travis, *Shock Initiation of Detonation in Liquid Explosives.* Physics of Fluids, 1961. **4**(4): p. 498-510.
4. Field, J.E., G.M. Swallowe, and S.N. Heavens, *Ignition Mechanisms of Explosives during Mechanical Deformation.* Proceedings of the Royal Society of London. A. Mathematical and Physical Sciences, 1982. **382**(1782): p. 231-244.
5. Field, J.E., *Hot spot ignition mechanisms for explosives.* Accounts of chemical research, 1992. **25**(11): p. 489-496.
6. Kim, S., Wei, Y., Horie, Y., Zhou, M., *Prediction of shock initiation thresholds and ignition probability of polymer-bonded explosives using mesoscale simulations.* Journal of the Mechanics and Physics of Solids, 2018. **114**: p. 97-116.
7. Barua, A., *Mesoscale computational prediction and quantification of thermomechanical ignition behavior of polymer-bonded explosives (PBXs)*, in *Mechanical Engineering*. 2013, Georgia Institute of Technology: Atlanta, GA. p. 264.

8. Yarrington, C., R.R. Wixom, and D.L. Damm, *Mesoscale Simulations Using Realistic Microstructure and First Principles Equation of State*. 2012, Sandia National Lab.(SNL-NM), Albuquerque, NM (United States). p. 10.
9. Baer, M.R., *Modeling heterogeneous energetic materials at the mesoscale.* Thermochimica Acta, 2002. **384**(1-2): p. 351-367.
10. Wood, M.A., Kittell, D.E., Yarrington, C.D., Thompson, A.P., *Multiscale modeling of shock wave localization in porous energetic material.* Physical Review B, 2018. **97**(1): p. 014109.
11. Miller, C., Kittell, D.E., Yarrington, C.D., Zhou, M., *Prediction of Probabilistic Detonation Threshold via Millimeter-Scale Microstructure-Explicit and Void-Explicit Simulations.* Prop., Explos., Pyrotech..2020. **45**(2): p. 254-269.
12. Yarrington, C.D., R.R. Wixom, and D.L. Damm, *Shock interactions with heterogeneous energetic materials.* Journal of Applied Physics, 2018. **123**(10): p. 105901.
13. An, Q., Goddard, W.A., Zybin, S.V., Luo, S.-N.., *Inhibition of Hotspot Formation in Polymer Bonded Explosives Using an Interface Matching Low Density Polymer Coating at the Polymer–Explosive Interface.* Journal of Physical Chemistry C, 2014. **118**(34): p. 19918–19928.
14. Rai, N.K., Sen, O., and Udaykumar, H.S., *Macro-scale sensitivity through meso-scale hotspot dynamics in porous energetic materials: Comparing the shock response of 1,3,5-triamino-2,4,6-trinitrobenzene (TATB) and 1,3,5,7-tetranitro-1,3,5,7-tetrazoctane (HMX).* Journal of Applied Physics, 2020. **128**(8): p. 085903.
15. Bassett, W.P., et al., *Shock initiation of explosives: High temperature hot spots explained.* Applied Physics Letters, 2017. **111**(6): p. 061902.
16. Gustavsen, R.L., et al., *Double Shock Initiation of the HMX Based Explosive EDC-37.* Proceedings of the Conference of the American Physical Society, Topical Group on Shock Compression of Condensed Matter, Proceedings of a conference held in Atlanta, Georgia, 24-29 June 2001, 2002. **620**(1): p. 999-1002.
17. Vandersall, K.S., et al., *SHOCK INITIATION EXPERIMENTS ON THE HMX BASED EXPLOSIVE LX-10 WITH ASSOCIATED IGNITION AND GROWTH MODELING.* AIP Conference Proceedings, 2007. **955**(1): p. 1010-1013.
18. Dick, J.J., *Measurement of the shock initiation sensitivity of low density HMX.* Combustion and Flame, 1983. **54**(1-3): p. 121-129.
19. Garcia, F., Vandersall, K.S., and Tarver, C.M., *Shock initiation experiments with ignition and growth modeling on low density HMX.* Journal of Physics: Conference Series, 2014. **500**(5): p. 052048.
20. Tringe, J.W., et al., *Observation and modeling of deflagration-to-detonation transition (DDT) in low-density HMX.* AIP Conference Proceedings, 2017. **1793**(1): p. 060024.
21. Skidmore, C.B., et al. *The evolution of microstructural changes in pressed HMX explosives*. 1998. (No. LA-UR-98-3473; CONF-980803-). Los Alamos National Lab., NM (United States).
22. Ilavsky, J., Allen, A.J., Long, G.G., Jemian, P.R., *Effective pinhole-collimated ultrasmall-angle x-ray scattering instrument for measuring anisotropic microstructures.* Review of Scientific Instruments, 2002. **73**(3): p. 1660-1662.
23. Allen, A.J., *Characterization of Ceramics by X-Ray and Neutron Small-Angle Scattering.* Journal of the American Ceramic Society, 2005. **88**(6): p. 1367-1381.
24. Stepanov, V., et al., *Structural Characterization of RDX-Based Explosive Nanocomposites.* Propellants, Explosives, Pyrotechnics, 2013. **38(3): p**. 386-393.
25. Willey, T.M., et al., *Mesoscale evolution of voids and microstructural changes in HMX-based explosives during heating through the β-δ phase transition.* Journal of Applied Physics, 2015. **118**(5): p. 055901.
26. Willey, T.M., et al., *Changes in Pore Size Distribution upon Thermal Cycling of TATB-based Explosives Measured by Ultra-Small Angle X-Ray Scattering.* Prop., Explos., Pyrotech., 2006. **31**(6): p. 466-471.
27. Mang, J.T. and Hjelm, R.P., *Preferred Void Orientation in Uniaxially Pressed PBX 9502.* Prop., Explos., Pyrotech., 2021. **46**(1): p. 67-77.
28. Li, C., Hamilton, B.W., and Strachan, A., *Hotspot formation due to shock-induced pore collapse in 1,3,5,7-tetranitro-1,3,5,7-tetrazoctane (HMX): Role of pore shape and shock strength in collapse mechanism and temperature.* Journal of Applied Physics, 2020. **127**(17): p. 175902.
29. Austin, R.A., Barton, N.R., Howard, W.M., Fried, L.E., *Modeling pore collapse and chemical reactions in shock-loaded HMX crystals.* Journal of Physics: Conference Series, 2014. **500**(5): p. 052002.
30. Springer, H.K., et al., *Modeling the effects of shock pressure and pore morphology on hot spot mechanisms in HMX.* Prop., Explos., Pyrotech., 2018. **43**(8): p. 805-817.

31. Kapahi, A. and H. Udaykumar, *Three-dimensional simulations of dynamics of void collapse in energetic materials.* Shock Waves, 2015. **25**(2): p. 177-187.
32. Rai, N.K. and Udaykumar, H., *Mesoscale simulation of reactive pressed energetic materials under shock loading.* Journal of Applied Physics, 2015. **118**(24): p. 245905.
33. Rai, N.K. and Udaykumar, H., *Three-dimensional simulations of void collapse in energetic materials.* Physical Review Fluids, 2018. **3**(3): p. 033201.
34. Sen, O., et al., *Multi-scale shock-to-detonation simulation of pressed energetic material: A meso-informed ignition and growth model.* Journal of Applied Physics, 2018. **124**(8): p. 085110.
35. Molek, C.D., et al., *Microstructural Characterization of Pressed HMX Material Sets at Differing Densities.* Shock Compression of Condensed Matter - 2015, AIP Conf. Proc. 1793, 040007 (2017)
36. Welle, E.J., Molek, C.D., Wixom, R.R., Samuels, P., *Microstructural effects on the ignition behavior of HMX.* Journal of Physics: Conference Series, 2014. **500**(5): p. 052049.
37. Welle, E.J., Wixom, R.R., Molek, C.D., Samuels, P., *Microstructural effects on the ignition behavior of various HMX materials-report SAND2013-5308C.* 2013, Sandia National Lab.(SNL-NM), Albuquerque, NM (United States). p. 1.
38. Miller, C., Olsen, D., Wei, Y., Zhou, M., *Three-dimensional microstructure-explicit and void-explicit mesoscale simulations of detonation of HMX at millimeter sample size scale.* Journal of Applied Physics, 2020. **127**(12): p. 125105.
39. McGlaun, J.M., Thompson, S.L., Elrick, M.G., *CTH: A three-dimensional shock wave physics code,*. International Journal of Impact Engineering, 1990. **10**(1-4): p. 351-360.
40. Jaw, K.S. and Lee, J.S., *Thermal behaviors of petn base polymer bonded explosives.* Journal of Thermal Analysis and Calorimetry, 2008. **93**(3): p. 953-957.
41. Chaturvedi, S. and Dave, P.N., *Solid propellants: AP/HTPB composite propellants.* Arabian Journal of Chemistry, 2019. **12**(8): p. 2061-2068.
42. Kerley, G.I., *Hydrocode Calculations of Detonator/Booster Initiation by Fragment Impacts.* 1997, Sandia National Lab.(SNL-NM), Albuquerque, NM (United States): p. 1-50.
43. Wei, Y., Kim, S., Horie, Y., Zhou, M., *Quantification of probabilistic ignition thresholds of polymer-bonded explosives with microstructure defects.* Journal of Applied Physics, 2018. **124**(16): p. 165110.
44. Skidmore, C.B., Phillips, D.S., Son, S.F., Asay, B.W., *Characterization of HMX particles in PBX 9501*. AIP Conf. Proc. 429, 579-582 (1998).
45. Kim, S., Barua, A., Horie, Y., Zhou, M., *Ignition probability of polymer-bonded explosives accounting for multiple sources of material stochasticity.* Journal of Applied Physics, 2014. **115**(17): p. 174902.
46. Das, P., et al., *Molecular dynamics-guided material model for the simulation of shock-induced pore collapse in β-octahydro-1,3,5,7-tetranitro-1,3,5,7-tetrazocine (β-HMX).*. Journal of Applied Physics, 2021. 1**30**(8): p. 085901.
47. Zhai, M., and McKenna, G.B. *Mechanical properties of pentaerythritol tetranitrate(PETN) single crystals from nano-indentation: Depth dependent response at the nano meter scale.* Crystal Research and Technology, 2016. **51**(7): p. 414-427.
48. Hertel, E.S. and G.I. Kerley, *CTH EOS Package: Introductory Tutorial, Sandia National Laboratories report SAND98-0945*. 1998, Sandia National Lab.(SNL-NM), Albuquerque, NM (United States).
49. Burnham, A.K., Weese, R.K., and Andrzejewski, W.J., *Kinetics of HMX and CP Decomposition and Their Extrapolation for Lifetime Assessment.* 36th International Annual Conf & 32nd Intl Pyrotechnics Seminar Conf. Proc. in Karlruhe, Germany, 2005.
50. Laidler, K.J., *The development of the Arrhenius equation.* Journal of Chemical Education, 1984. **61**(6): p. 494.
51. Springer, H.K., Tarver, C.M., Reaugh, J.E., May, C.M., *Investigating short-pulse shock initiation in HMX-based explosives with reactive meso-scale simulations.* Journal of Physics: Conference Series, 2014. **500**(5): p. 052041.
52. Tarver, C.M., May, C.M., *Short pulse shock initiation experiments and modeling on LX-16, LX-10, and ultrafine TATB*. Fourteenth International Detonation Symposium, IDS 2010. p. 648-654.
53. Miller, C., Kittell, D.E., Yarrington, C.D., Zhou, M., *Prediction of Probabilistic Detonation Threshold via Millimeter-Scale Microstructure-Explicit and Void-Explicit Simulations.* Propellants, Explosives, Pyrotechnics, 2020. **45**(2): p. 254-269.
54. Lee, E.L. and Tarver, C.M., *Phenomenological model of shock initiation in heterogeneous explosives.* Physics of Fluids, 1980. **23**(12): p. 2362-2372.

55. Tarver, C.M., *Chemical energy release in self-sustaining detonation waves in condensed explosives.* Combustion and Flame, 1982. **46**: p. 648-654.
56. Mulford, R.N. and Swift, D.C., *Mesoscale modelling of shock initiation in HMX-based explosives.* AIP Conf. Proc., 2002. **620**(1): p. 415-418.
57. Rimoli, J.J., Gürses, E., and Ortiz, M., *Shock-induced subgrain microstructures as possible homogenous sources of hot spots and initiation sites in energetic polycrystals.* Physical Review B, 2010. **81**(1): p. 014112.
58. Bennett, J.G., Haberman, K.S., Johnson, J.N., Asay, B.W., *A constitutive model for the non-shock ignition and mechanical response of high explosives.* Journal of the Mechanics and Physics of Solids, 1998. **46**(12): p. 2303-2322.
59. Benson, D.J. and Conley, P., *Eulerian finite-element simulations of experimentally acquired HMX microstructures.* Modelling and Simulation in Materials Science and Engineering, 1999. **7**(3): p. 333-354.
60. Rao, P.T., and Gonthier, K.A., *Analysis of Dissipation Induced by Successive Planar Shock Loading of Granular Explosive*, in 51st AIAA/SAE/ASEE Joint Propulsion Conference Proceeding. 2015. Orlando, FL.
61. Mader, C.L., *Numerical modeling of detonations.* Los Alamos Series in Basic and Applied Sciences, Berkeley: University of California Press, 1979.
62. Borne, L., *in 10th International Symposium on Detonation (Office of Naval Research, 1993).* 1993: p. 286.
63. Peterson, J.R. and Wight, C.A., *An Eulerian–Lagrangian computational model for deflagration and detonation of high explosives.* Combustion and Flame, 2012. **159**(7): p. 2491-2499.
64. Cheng, T., *Review of novel energetic polymers and binders - high energy propellant ingredients for the new space race.* Designed Monomers and Polymers, 2019. **22**(1): p. 54-65.